

Self-supervised 3D anatomy segmentation using self-distilled masked image transformer (SMIT)

Jue Jiang¹, Neelam Tyagi¹, Kathryn Tringale², Christopher Crane², and Harini Veeraraghavan¹

¹ ¹ Department of Medical Physics, Memorial Sloan Kettering Cancer Center

² ² Department of Radiation Oncology, Memorial Sloan Kettering Cancer Center

veerarah@mskcc.org

Abstract. Vision transformers, with their ability to more efficiently model long-range context, have demonstrated impressive accuracy gains in several computer vision and medical image analysis tasks including segmentation. However, such methods need large labeled datasets for training, which is hard to obtain for medical image analysis. Self-supervised learning (SSL) has demonstrated success in medical image segmentation using convolutional networks. In this work, we developed a self-distillation learning with masked image modeling method to perform SSL for vision transformers (SMIT) applied to 3D multi-organ segmentation from CT and MRI. Our contribution is a dense pixel-wise regression within masked patches called masked image prediction, which we combined with masked patch token distillation as pretext task to pre-train vision transformers. We show our approach is more accurate and requires fewer fine tuning datasets than other pretext tasks. Unlike prior medical image methods, which typically used image sets arising from disease sites and imaging modalities corresponding to the target tasks, we used 3,643 CT scans (602,708 images) arising from head and neck, lung, and kidney cancers as well as COVID-19 for pre-training and applied it to abdominal organs segmentation from MRI pancreatic cancer patients as well as publicly available 13 different abdominal organs segmentation from CT. Our method showed clear accuracy improvement (average DSC of 0.875 from MRI and 0.878 from CT) with reduced requirement for fine-tuning datasets over commonly used pretext tasks. Extensive comparisons against multiple current SSL methods were done. Code will be made available upon acceptance for publication. ³

Keywords: Self-supervised learning, segmentation, self-distillation, masked image modeling, masked embedding transformer

1 Introduction

Vision transformers (ViT)[1] efficiently model long range contextual information using multi-head self attention mechanism, which makes them robust to occlusions, image noise, as well as domain and image contrast differences. ViTs have

³ [This paper has been early accepted by MICCAI 2022.](#)

shown impressive accuracy gains over convolutional neural networks (CNN) in medical image segmentation[2,3]. However, ViT training requires a large number of expert labeled training datasets that are not commonly available in medical image applications. Self-supervised learning (SSL) overcomes the requirement for large labeled training datasets by using large unlabeled datasets through pre-defined annotation free pretext tasks. The pretext tasks are based on modeling visual information contained in images and provide a surrogate supervision signal for feature learning[4,5,6]. Once pre-trained, the model can be re-purposed for a variety of tasks and require relatively few labeled sets for fine-tuning.

The choice of pretext tasks is crucial to successfully mine useful image information using SSL. Pretext tasks in medical image applications typically focus on learning denoising autoencoders constructed with CNNs to recover images in the input space using corrupted versions of the original images[7,8]. Various data augmentation strategies have been used to corrupt images, which include jigsaw puzzles[9,10], transformation of image contrast and local texture[7], image rotations[5], and masking of whole image slices[11]. Learning strategies include pseudo labels[8,12,13] and contrastive learning[9,14,15,16]. However, CNNs are inherently limited in their capacity to model long-range context than transformers, which may reduce their robustness to imaging variations and contrast differences. Hence, we combined ViT with SSL using masked image modeling (MIM) and self-distillation of concurrently trained teacher and student networks.

MIM has been successfully applied to transformers to capture local context while preserving global semantics in natural image analysis tasks[17,18,19,20,19,21]. Knowledge distillation with concurrently trained teacher has also been used for medical image segmentation by leveraging different imaging modality datasets (CT and MRI)[22,23]. Self-distillation on the other hand, uses different augmented views of the same image[24] and has been used with contrastive learning with convolutional encoders for medical image classification[13].

Self-distillation learning with MIM and using a pair of online teacher and a student transformer encoders have been used for natural image classification and segmentation[19,24]. However, the pretext tasks focused only on extracting global image embedding as class tokens [CLS][24], which was improved with global and local patch token embeddings [19]. However, these methods ignored the dense pixel dependencies, which is essential for dense prediction tasks like segmentation. Hence, we introduced a masked image prediction (MIP) pretext task to predict pixel-wise intensities within masked patches combined with the local and global embedding distillation applied to medical image segmentation.

Our contributions include: (i) SSL using MIM and self-distillation approach combining masked image prediction, masked patch token distillation, and global image token distillation for CT and MRI organs segmentation using transformers. (ii) a simple linear projection layer for medical image reconstruction to speed up pre-training, which we show is more accurate than multi-layer decoder. (iii) SSL pre-training using large 3,643 3D CTs arising from a variety of disease sites including head and neck, chest, and abdomen with different cancers (lung, naso/oropharynx, kidney) and COVID-19 applied to CT and MRI segmentation.

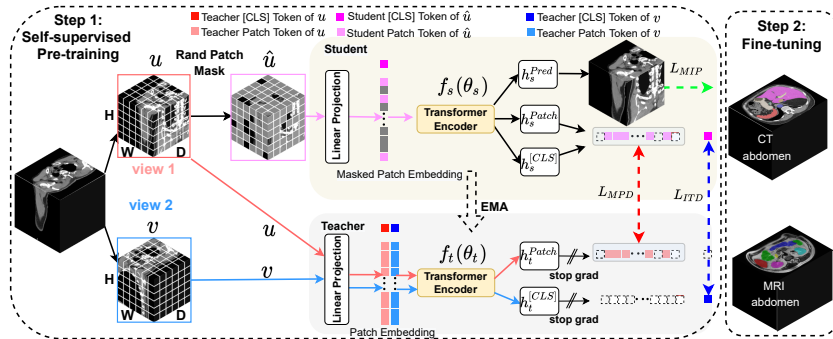


Fig. 1: SMIT: Self-distillation with masked image modeling for transformers using SSL.

(iv) Evaluation of various pretext tasks using transformer encoders related to fine tuning data size requirements and segmentation accuracy.

2 Method

Goal: Extract a universal representation of images for dense prediction tasks, given an unlabeled dataset of Q images.

Approach: A visual tokenizer $f_s(\theta_s)$ implemented as a transformer encoder is learned via self-distillation using MIM pretext tasks in order to convert an image x into image tokens $\{x_i\}_{i=1}^N$, N being the sequence length. Self distillation is performed by concurrently training an online teacher tokenizer model $f_t(\theta_t)$ with the same network structure as $f_s(\theta_s)$ serving as the student model. A global image token distillation (ITD) is performed as a pretext task to match the global tokens extracted by f_t and f_s as done previously[24]. MIM pretext tasks include masked image prediction (MIP) and masked patch token distillation (MPD).

Suppose $\{u, v\}$ are two augmented views of a 3D image x . N image patches are extracted from the images to create a sequence of image tokens[1], say $u = \{u_i\}_{i=1}^N$. The image tokens are then corrupted by randomly masking image tokens based on a binary vector $m = \{m_i\}_{i=1}^N \in \{0, 1\}$ with a probability p and then replacing with mask token[20] $e_{[MASK]}$ such that as $\tilde{u} = m \odot u$ with $\tilde{u}_i = e_{[MASK]}$ at $m_i = 1$ and $\tilde{u}_i = u_i$ at $m_i = 0$. The second augmented view v is also corrupted but using a different mask vector instance m' as $\tilde{v} = m' \odot v$.

Dense pixel dependency modeling using MIP: MIP involves recovering the original image view u from corrupted \tilde{u} , as $\hat{u} = h_s^{Pred}(f_s(\tilde{u}, \theta_s))$, where h_s^{Pred} decodes the visual tokens produced by a visual tokenizer $f_s(\theta_s)$ into images (see Fig.1). MIP involves dense pixel regression of image intensities within masked patches using the context of unmasked patches. The MIP loss is computed as (dotted green arrow in Fig.1):

$$L_{MIP} = \sum_i^N E \|m_i \cdot (h_s^{Pred}(f_s(\tilde{u}_i, \theta_s))) - u_i\|_1 \quad (1)$$

h_s^{Pred} is a linear projection with one layer for dense pixel regression. A symmetrized loss using v and \tilde{v} is combined to compute the total loss for L_{MIP} .

Masked patch token self-distillation (MPD): MPD is accomplished by optimizing a teacher $f_t(\theta_t)$ and a student visual tokenizer $f_s(\theta_s)$ such that the student network predicts the tokens of the teacher network. The student network f_s tokenizes the corrupted version of an image \tilde{u} to generate visual tokens $\phi' = \{\phi'_i\}_{i=1}^N$. The teacher network f_t tokenizes the uncorrupted version of the same image u to generate visual tokens $\phi = \{\phi_i\}_{i=1}^N$. Similar to MIP, MPD is only concerned with ensuring prediction of the masked patch tokens. Therefore, the loss is computed from masked portions (i.e. $m_i=1$) using cross-entropy of the predicted patch tokens (dotted red arrow in Fig.1):

$$L_{MPD} = - \sum_{i=1}^N m_i \cdot P_t^{Patch}(u_i, \theta_t) \log(P_s^{Patch}(\tilde{u}_i, \theta_s)), \quad (2)$$

where P_s^{Patch} and P_t^{Patch} are the patch token distributions for student and teacher networks. They are computed by applying *softmax* to the outputs of h_s^{Patch} and h_t^{Patch} . The sharpness of the token distribution is controlled using a temperature term $\tau_s > 0$ and $\tau_t > 0$ for the student and teacher networks, respectively. Mathematically, such a sharpening can be expressed as (using notation for the student network parameters) as:

$$P_s^{Patch}(u, \theta_s) = \frac{\exp(h_s^{Patch}(f_s(u_j, \theta_s))/\tau_s)}{\sum_{j=1}^K \exp(h_s^{Patch}(f_s(u_j, \theta_s))/\tau_s)}. \quad (3)$$

A symmetrized cross entropy loss corresponding to the other view v and \tilde{v} is also computed and averaged to compute the total loss for MPD.

Global image token self-distillation (ITD): ITD is done by matching the global image embedding represented as class tokens [CLS] distribution $P_s^{[CLS]}$ extracted from the corrupted view \tilde{u} by student using $h_s^{[CLS]}(f_s(\theta_s, \tilde{u}))$ with the token distribution $P_t^{[CLS]}$ extracted from the uncorrupted and different view v by the teacher using $h_t^{[CLS]}(f_t(\theta_t, v))$ (shown by dotted blue arrow in Fig.1) as:

$$L_{ITD} = - \sum_{i=1}^N m_i \cdot P_t^{[CLS]}(v_i, \theta_t) \log(P_s^{[CLS]}(\tilde{u}_i, \theta_s)) \quad (4)$$

Sharpening transforms are applied to $P_t^{[CLS]}$ and $P_s^{[CLS]}$ similar to Equation 4. A symmetrized cross entropy loss corresponding to the corrupted view \tilde{v} and another u is also computed and averaged to compute the total loss for L_{ITD} .

Online teacher network update: Teacher network parameters were updated using exponential moving average (EMA) with momentum update, and shown to be feasible for SSL[24,19] as: $\theta_t = \lambda_m \theta_t + (1 - \lambda_m) \theta_s$, where λ_m is momentum, which was updated using a cosine schedule from 0.996 to 1 during training. The total loss was, $L_{total} = L_{MIP} + \lambda_{MPD} L_{MPD} + \lambda_{ITD} L_{ITD}$.

Implementation details: All the networks were implemented using the Pytorch library and trained on 4 Nvidia GTX V100. SSL optimization was done using ADAMw with a cosine learning rate scheduler trained for 400 epochs with an initial learning rate of 0.0002 and warmup for 30 epochs. $\lambda_{MPD}=0.1$, $\lambda_{ITD}=0.1$ were set experimentally. A default mask ratio of 0.7 was used. Centering and sharpening operations reduced chances of degenerate solutions[24]. τ_s was

Table 1: Accuracy on BTCV standard challenge test set. SP: spleen, RK/LK: right & left kidney, GB: gall bladder, ESO: esophagus, LV: liver, STO: stomach, AOR: aorta, IVC: inferior vena cava, SPV: portal & splenic vein, Pan: Pancreas, AG: Adrenals.

Method	SP	RK	LK	GB	ESO	LV	STO	AOR	IVC	SPV	Pan	AG	AVG
ASPP[29]	0.935	0.892	0.914	0.689	0.760	0.953	0.812	0.918	0.807	0.695	0.720	0.629	0.811
nnUnet[30]	0.942	0.894	0.910	0.704	0.723	0.948	0.824	0.877	0.782	0.720	0.680	0.616	0.802
TrsUnet[31]	0.952	0.927	0.929	0.662	0.757	0.969	0.889	0.920	0.833	0.791	0.775	0.637	0.838
CoTr[2]	0.958	0.921	0.936	0.700	0.764	0.963	0.854	0.920	0.838	0.787	0.775	0.694	0.844
UNETR[3]	0.968	0.924	0.941	0.750	0.766	0.971	0.913	0.890	0.847	0.788	0.767	0.741	0.856
SMIT(rand)	0.959	0.921	0.947	0.746	0.802	0.972	0.916	0.917	0.848	0.797	0.817	0.711	0.850
SMIT(SSL)	0.967	0.945	0.948	0.826	0.822	0.976	0.934	0.921	0.864	0.827	0.851	0.754	0.878

set to 0.1 and τ_t was linearly warmed up from 0.04 to 0.07 in the first 30 epochs. SWIN-small backbone[25] with 768 embedding, window size of $4 \times 4 \times 4$, patch size of 2 was used. The 1-layer decoder was implemented with a linear projection layer with the same number of output channels as input image size. The network had 28.19M parameters. Following pre-training, only the student network was retained for fine-tuning and testing.

3 Experiments and Results

Training dataset: SSL pre-training was performed using 3,643 CT patient scans containing 602,708 images. Images were sourced from patients with head and neck (N=837) and lung cancers (N=1455) from internal and external[26], as well as those with kidney cancers[27] (N=710), and COVID-19[28] (N=650). GPU limitation was addressed for training, fine-tuning, and testing by image resampling ($1.5 \times 1.5 \times 2$ mm voxel size) and cropping ($128 \times 128 \times 128$) to enclose the body region. Augmented views for SSL training was produced through randomly cropped $96 \times 96 \times 96$ volumes, which resulted in $6 \times 6 \times 6$ image patch tokens. A sliding window strategy with half window overlap was used for testing[2,3].

CT abdomen organ segmentation (Dataset I): The pre-trained networks were fine-tuned to generate volumetric segmentation of 13 different abdominal organs from contrast-enhanced CT (CECT) scans using publicly available beyond the cranial vault (BTCV)[32] dataset. Randomly selected 21 images are used for training and the remaining used for validation. Furthermore, blinded testing of 20 CECTs evaluated on the grand challenge website is also reported.

MRI upper abdominal organs segmentation (Dataset II): The SSL network was evaluated for segmenting abdominal organs at risk for pancreatic cancer radiation treatment, which included stomach, small and large bowel, liver, and kidneys. No MRI or pancreatic cancer scans were used for SSL pre-training. Ninety two 3D T2-weighted MRIs (TR/TE = 1300/87 ms, voxel size of $1 \times 1 \times 2$ mm³, FOV of $400 \times 450 \times 250$ mm³) and acquired with pneumatic compression belt to suppress breathing motion were analyzed. Fine tuning used five-fold cross-validation and results from the validation folds not used in training are reported.

Experimental comparisons: SMIT was compared against representative SSL medical image analysis methods. Results from representative published methods on the BTCV testing set[30,2,3] are also reported. The SSL comparison methods

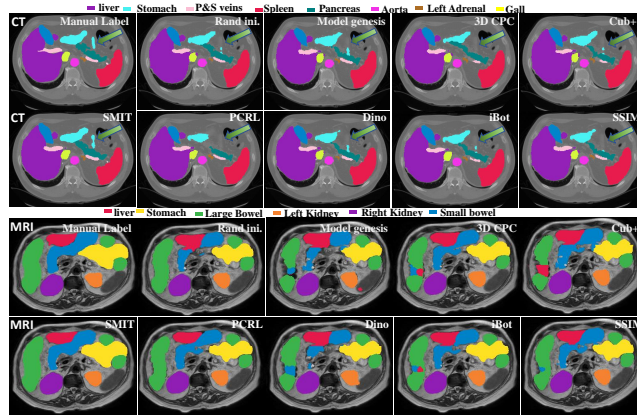


Fig. 2: Segmentation performance of different methods on MRI abdomen organs.

were chosen to evaluate the impact of the pretext task on segmentation accuracy and included (a) local texture and semantics modeling using model genesis[7], (b) jigsaw puzzles[10], (c) contrastive learning[16] with (a),(b), (c) implemented on CNN backbone, (d) self-distillation using whole image reconstruction[24], (e) masked patch reconstruction[18] without self-distillation, (f) MIM using self-distillation[19] with (d),(e), and (f) implemented in a SWIN transformer backbone. Random initialization results are shown for benchmarking purposes using both CNN and SWIN backbones. Identical training and testing sets were used with hyper-parameter adopted from their default implementation.

CT segmentation accuracy: As shown in Table.1, our method SMIT outperformed representative published methods including transformer-based segmentation[31,3,2]. SMIT was also more accurate than all evaluated SSL methods (Table.2) for most organs. Prior-guided contrast learning (PRCL)[16] was more accurate than SMIT for gall bladder (0.797 vs. 0.787). SMIT was more accurate than self-distillation with MIM[19] (average DSC of 0.848 vs. 0.833) as well as masked image reconstruction without distillation[18] (0.848 vs. 0.830). Fig.2 shows a representative case with multiple organs segmentations produced by the various methods. SMIT was the most accurate method including for organs with highly variable appearance and size such as the stomach and esophagus.

MRI segmentation accuracy: SMIT was more accurate than all other SSL-based methods for all evaluated organs, including stomach and bowels, which depict highly variable appearance and sizes (Table.2). SMIT was least accurate for small bowel compared to other organs, albeit this accuracy for small bowel was higher than all other methods. Fig.2 shows a representative case with multiple organs segmentations produced by the various methods.

Ablation experiments: All ablation and design experiments (1layer decoder vs. multi-layer or ML decoder) were performed using the BTCV dataset and used the SWIN-backbone as used for SMIT. ML decoder was implemented with five transpose convolution layers for up-sampling back to the input image resolution. Fig.4 shows the accuracy comparisons of networks pre-trained with different tasks including full image reconstruction, contrastive losses, pseudo labels[33],

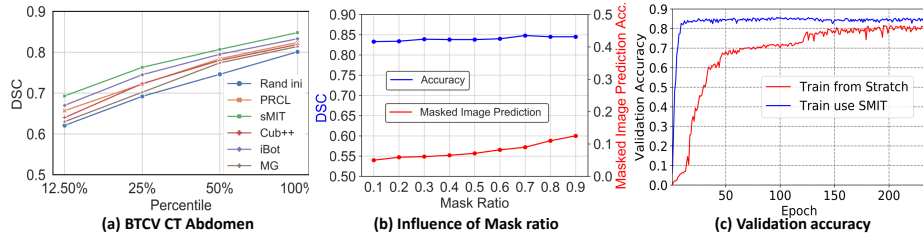


Fig. 3: (a) Impact of SSL task on fine-tuning sizes, (b) impact of mask ratio on masked image prediction and segmentation accuracy, (c) training convergence.

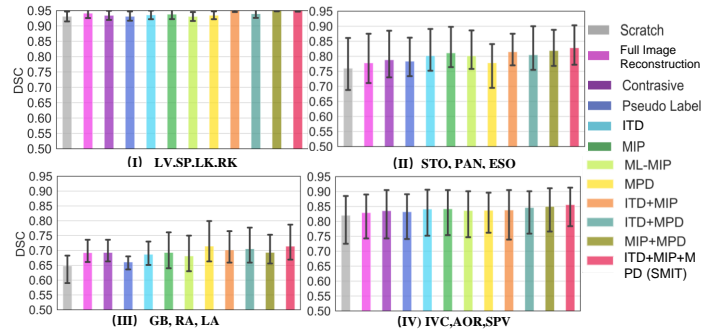


Fig. 4: Accuracy variations by organ types using different pretext tasks.

and various combination of the losses (L_{MIP} , L_{MPD} , L_{ITD}). As shown, the accuracies for all the methods was similar for large organs depicting good contrast that include liver, spleen, left and right kidney (Fig.4(I)). On the other hand, organs with low soft tissue contrast and high variability (Fig.4(II)) and small organs (Fig.4(III)) show larger differences in accuracies between methods with SMIT achieving more accurate segmentations. Major blood vessels Fig.4(IV) also depict segmentation accuracy differences across methods, albeit less so than for small organs and those with low soft-tissue contrast. Importantly, both full image reconstruction and multi-layer decoder based MIP (ML-MIP) were less accurate than SMIT, which uses masked image prediction with 1-layer linear projection decoder (Fig.4 (II,III,IV)). MPD was the least accurate for organs with low soft-tissue contrast and high variability (Fig.4(II)), which was improved slightly by adding global image distillation (ITD). MIP alone (using 1-layer decoder) was similarly accurate as SMIT and more accurate than other pretext task based segmentation including ITD[24], MPD+ITD[19].

Impact of pretext tasks on sample size for fine tuning: SMIT was more accurate than all other SSL methods irrespective of sample size used for fine-tuning (Fig.3(a)) and achieved faster convergence (Fig.3(c)). It outperformed iBot[19], which uses MPD and ITD, indicating effectiveness of MIP for SSL.

Impact of mask ratio on accuracy: Fig.3(b) shows the impact of mask ratio (percentage of masked patches) in the corrupted image for both the accuracy of masked image reconstruction (computed as mean square error [MSE]) as well as segmentation (computed using DSC metric). Increasing the mask ratio

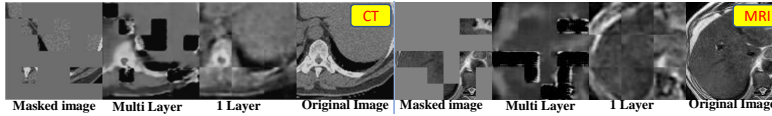


Fig. 5: Reconstructed images using 1-layer vs. multi-layer decoder trained with SMIT from masked images (0.7 masking ratio).

initially increased accuracy and then stabilized. Image reconstruction error increased slightly with increasing masking ratio. Fig.5 shows a representative CT and MRI reconstruction produced using default and multi-layer decoder, wherein our method was more accurate even in highly textured portions of the images containing multiple organs (additional examples are shown in Supplementary Fig 1). Quantitative comparisons showed our method was more accurate (MSE of 0.061 vs. 0.32) for CT (N=10 cases) and 92 MRI (MSE of 0.062 vs. 0.34) than multi-layer decoder.

Table 2: CT and MRI segmentation accuracy comparisons to SSL methods. Rand-random; LB-Large bowel, SB - Small bowel.

Mod	Organ	CNN					SWIN				
		Rand	MG[7]	CPC[9]	Cub++[34]	PRCL[16]	Rand	DINO[24]	iBOT[19]	SSIM[18]	SMIT
CT	Sp	0.930	0.950	0.940	0.926	0.937	0.944	0.946	0.948	0.950	0.963
	RK	0.892	0.934	0.916	0.928	0.919	0.926	0.931	0.936	0.934	0.950
	LK	0.894	0.918	0.903	0.914	0.921	0.905	0.913	0.919	0.913	0.943
	GB	0.605	0.639	0.718	0.715	0.797	0.694	0.730	0.777	0.761	0.787
	ESO	0.744	0.739	0.756	0.768	0.759	0.732	0.752	0.760	0.772	0.772
	LV	0.947	0.967	0.953	0.946	0.954	0.950	0.954	0.956	0.956	0.970
	STO	0.862	0.879	0.896	0.881	0.877	0.861	0.891	0.900	0.898	0.903
	AOR	0.875	0.909	0.900	0.892	0.894	0.885	0.906	0.901	0.905	0.913
	IVC	0.844	0.882	0.855	0.866	0.851	0.851	0.866	0.879	0.867	0.871
	SPV	0.727	0.739	0.731	0.734	0.760	0.725	0.752	0.759	0.754	0.784
	Pan	0.719	0.706	0.726	0.731	0.693	0.688	0.763	0.755	0.764	0.810
	RA	0.644	0.671	0.655	0.665	0.661	0.660	0.651	0.659	0.640	0.669
LA	0.648	0.640	0.655	0.675	0.680	0.590	0.680	0.681	0.678	0.687	
	AVG.	0.795	0.813	0.816	0.819	0.823	0.801	0.826	0.833	0.830	0.848
MR	LV	0.921	0.936	0.925	0.920	0.930	0.922	0.920	0.939	0.937	0.942
	LB	0.786	0.824	0.824	0.813	0.823	0.818	0.804	0.833	0.835	0.855
	SB	0.688	0.741	0.745	0.735	0.745	0.708	0.729	0.744	0.759	0.775
	STO	0.702	0.745	0.769	0.783	0.793	0.732	0.750	0.783	0.775	0.812
	LK	0.827	0.832	0.876	0.866	0.876	0.837	0.911	0.883	0.874	0.936
	RK	0.866	0.886	0.863	0.861	0.871	0.845	0.896	0.906	0.871	0.930
		AVG.	0.798	0.827	0.834	0.830	0.840	0.810	0.835	0.848	0.842

4 Discussion and conclusion

In this work, we demonstrated the potential for SSL with 3D transformers for medical image segmentation. Our approach, which leverages CT volumes arising from highly disparate body locations and diseases showed feasibility to produce robustly accurate segmentations from CT and MRI scans and surpassed multiple current SSL-based methods, especially for hard to segment organs with high

appearance variability and small sizes. Our introduced masked image dense prediction pretext task improved the ability of self distillation using MIM to segment a variety of organs from CT and MRI and with lower requirement of fine tuning dataset size. Our method shows feasibility for medical image segmentation.

5 Conclusion

References

1. Dosovitskiy, A., Beyer, L., Kolesnikov, A., Weissenborn, D., Zhai, X., Unterthiner, T., Dehghani, M., Minderer, M., Heigold, G., Gelly, S., Uszkoreit, J., Houlsby, N.: An image is worth 16x16 words: Transformers for image recognition at scale. In: International Conference on Learning Representations. (2021)
2. Xie, Y., Zhang, J., Shen, C., Xia, Y.: Cotr: Efficiently bridging cnn and transformer for 3d medical image segmentation. In: Medical Image Computing and Computer Assisted Intervention. (2021) 171–180
3. Hatamizadeh, A., Tang, Y., Nath, V., Yang, D., Myronenko, A., Landman, B., Roth, H., Xu, D.: Unetr: Transformers for 3d medical image segmentation (2021)
4. Noroozi, M., Favaro, P.: Unsupervised learning of visual representations by solving jigsaw puzzles. In: European conf. on computer vision, Springer (2016) 69–84
5. Komodakis, N., Gidaris, S.: Unsupervised representation learning by predicting image rotations. In: Intl Conf on Learning Representations (ICLR). (2018)
6. He, K., Fan, H., Wu, Y., Xie, S., Girshick, R.: Momentum contrast for unsupervised visual representation learning. In: Proceedings of the IEEE/CVF conference on CVPR. (2020) 9729–9738
7. Zhou, Z., Sodha, V., Pang, J., Gotway, M.B., Liang, J.: Models genesis. Medical image analysis **67** (2021) 101840
8. Haghighi, F., Taher, M.R.H., Zhou, Z., Gotway, M.B., Liang, J.: Learning semantics-enriched representation via self-discovery, self-classification, and self-restoration. In: International Conference on Medical Image Computing and Computer-Assisted Intervention, Springer (2020) 137–147
9. Taleb, A., Loetzsch, W., Danz, N., Severin, J., Gaertner, T., Bergner, B., Lippert, C.: 3d self-supervised methods for medical imaging. Advances in Neural Information Processing Systems **33** (2020) 18158–18172
10. Zhu, J., Li, Y., Hu, Y., Ma, K., Zhou, S.K., Zheng, Y.: Rubik’s cube+: A self-supervised feature learning framework for 3d medical image analysis. Medical image analysis **64** (2020) 101746
11. Jun, E., Jeong, S., Heo, D.W., Suk, H.I.: Medical transformer: Universal brain encoder for 3d mri analysis. arXiv preprint arXiv:2104.13633 (2021)
12. Chen, L., Bentley, P., Mori, K., Misawa, K., Fujiwara, M., Rueckert, D.: Self-supervised learning for medical image analysis using image context restoration. Medical image analysis **58** (2019) 101539
13. Sun, J., Wei, D., Ma, K., Wang, L., Zheng, Y.: Unsupervised representation learning meets pseudo-label supervised self-distillation: A new approach to rare disease classification. In: International Conference on Medical Image Computing and Computer-Assisted Intervention, Springer (2021) 519–529
14. Chaitanya, K., Erdil, E., Karani, N., Konukoglu, E.: Contrastive learning of global and local features for medical image segmentation with limited annotations. Advances in Neural Information Processing Systems **33** (2020) 12546–12558

15. Feng, R., Zhou, Z., Gotway, M.B., Liang, J.: Parts2whole: Self-supervised contrastive learning via reconstruction. In: Domain Adaptation and Representation Transfer, and Distributed and Collaborative Learning. Springer (2020) 85–95
16. Zhou, H.Y., Lu, C., Yang, S., Han, X., Yu, Y.: Preservational learning improves self-supervised medical image models by reconstructing diverse contexts. In: Proceedings of the IEEE/CVF International Conference on Computer Vision. (2021) 3499–3509
17. Li, Z., Chen, Z., Yang, F., Li, W., Zhu, Y., Zhao, C., Deng, R., Wu, L., Zhao, R., Tang, M., et al.: MST: Masked self-supervised transformer for visual representation. *Advances in Neural Information Processing Systems* **34** (2021)
18. Xie, Z., Zhang, Z., Cao, Y., Lin, Y., Bao, J., Yao, Z., Dai, Q., Hu, H.: SimMIM: A simple framework for masked image modeling. *arXiv preprint:2111.09886* (2021)
19. Zhou, J., Wei, C., Wang, H., Shen, W., Xie, C., Yuille, A., Kong, T.: Image BERT pre-training with online tokenizer. In: International Conference on Learning Representations. (2022)
20. Bao, H., Dong, L., Wei, F.: BEiT: BERT pre-training of image transformers. *arXiv preprint arXiv:2106.08254* (2021)
21. He, K., Chen, X., Xie, S., Li, Y., Dollár, P., Girshick, R.: Masked autoencoders are scalable vision learners. *arXiv preprint arXiv:2111.06377* (2021)
22. Li, K., Yu, L., Wang, S., Heng, P.A.: Towards cross-modality medical image segmentation with online mutual knowledge distillation. *Proc. AAAI* **34**(01) (Apr. 2020) 775–783
23. Jiang, J., Rimner, A., Deasy, J.O., Veeraraghavan, H.: Unpaired cross-modality educed distillation (cmedl) for medical image segmentation. *IEEE Transactions on Medical Imaging* (2021)
24. Caron, M., Touvron, H., Misra, I., Jégou, H., Mairal, J., Bojanowski, P., Joulin, A.: Emerging properties in self-supervised vision transformers. In: Proceedings of the IEEE/CVF International Conference on Computer Vision. (2021) 9650–9660
25. Liu, Z., Lin, Y., Cao, Y., Hu, H., Wei, Y., Zhang, Z., Lin, S., Guo, B.: Swin transformer: Hierarchical vision transformer using shifted windows. In: Proc. of the IEEE Int. Conf. on Computer Vision. (2021) 10012–10022
26. Aerts, H., E., R.V., Leijenaar, R.T., Parmar, C., Grossmann, P., Carvalho, S., Lambin, P.: Data from NSCLC-radiomics. *The Cancer Imaging Archive* (2015)
27. Akin, O., Elnajjar, P., Heller, M., Jarosz, R., Erickson, B., Kirk, S., Filippini, J.: Radiology data from the cancer genome atlas kidney renal clear cell carcinoma [tcga-kirc] collection. *The Cancer Imaging Archive* (2016)
28. Harmon, S.A., Sanford, T.H., Xu, S., Turkbey, E.B., Roth, H., Xu, Z., Yang, D., Myronenko, A., Anderson, V., Amalou, A., et al.: Artificial intelligence for the detection of covid-19 pneumonia on chest ct using multinational datasets. *Nature communications* **11**(1) (2020) 1–7
29. Chen, L.C., Zhu, Y., Papandreou, G., Schroff, F., Adam, H.: Encoder-decoder with atrous separable convolution for semantic image segmentation. In: Proceedings of the European conference on computer vision (ECCV). (2018) 801–818
30. Isensee, F., Jaeger, P.F., Kohl, S.A., Petersen, J., Maier-Hein, K.H.: nnu-net: a self-configuring method for deep learning-based biomedical image segmentation. *Nature methods* **18**(2) (2021) 203–211
31. Chen, J., Lu, Y., Yu, Q., Luo, X., Adeli, E., Wang, Y., Lu, L., Yuille, A.L., Zhou, Y.: Transunet: Transformers make strong encoders for medical image segmentation. *arXiv preprint arXiv:2102.04306* (2021)
32. Landman, B., Xu, Z., Igelsias, J., Styner, M., Langerak, T., Klein, A.: MICCAI multi-atlas labeling beyond the cranial vault–workshop and challenge (2015)

33. Chen, X., Xie, S., He, K.: An empirical study of training self-supervised vision transformers. In: Proceedings of the IEEE/CVF International Conference on Computer Vision. (2021) 9640–9649
34. Tao, X., Li, Y., Zhou, W., Ma, K., Zheng, Y.: Revisiting rubik’s cube: Self-supervised learning with volume-wise transformation for 3d medical image segmentation. In: International Conference on Medical Image Computing and Computer-Assisted Intervention, Springer (2020) 238–248